Computing low-frequency radar surface echoes for planetary radar using Huygens-Fresnel's principle

Yann Berquin, Alain Herique, Wlodek Kofman, Essam Heggy

AGU PUBLICATIONS

Radio Science

RESEARCH ARTICLE
10.1002/2015RS005714

Computing low-frequency radar surface echoes for planetary radar using Huygens-Fresnel's principle

Yann Berquin[1], Alain Herique[1], Wlodek Kofman[1,2], and Essam Heggy[3]

[1]UJF-Grenoble CNRS-INSU, Institut de Planétologie et d'Astrophysique de Grenoble UMR 5274, Grenoble, France, [2]Space Research Center, PAN, Warsaw, Poland, [3]Ming Hsieh Department of Electrical Engineering, Viterbi School of Engineering, University of Southern California, Los Angeles, California, USA

Key Points:
- Low-frequency radar surface echoes can be computed inexpensively
- Boundary integral formulation is well adapted for planetary radar data analysis

Correspondence to:
A. Herique,
alain.herique@obs.ujf-grenoble.fr

Citation:
Berquin, Y., A. Herique, W. Kofman, and E. Heggy (2015), Computing low-frequency radar surface echoes for planetary radar using Huygens-Fresnel's principle, *Radio Sci.*, *50*, 1097–1109, doi:10.1002/2015RS005714.

Received 24 MAR 2015
Accepted 16 SEP 2015
Accepted article online 21 SEP 2015
Published online 30 OCT 2015

Abstract Radar echoes from planetary sounders often contain ambiguities between surface echoes (clutter) and subsurface reflections. Such problems severely constrain quantitative data analysis especially for rough terrains. We propose a physical optics approach to simulate planetary sounding radar surface echoes to address this specific issue. The method relies on the Huygens-Fresnel's principle which permits the recasting of Maxwell's equations in a surface integral formulation. To compute this integral, we describe the surface through a mesh composed of adjacent triangular elements for which we provide an analytical expression of the scattered electromagnetic fields. The main contribution of this work lies in the use of analytical integrals over triangular facet elements much larger than the wavelength of the electromagnetic field. Hence, the advantage of the proposed approach is its computation efficiency which reduces the computational requirements while maintaining the physical optics accuracy. This allows a systematic analysis of the continuously growing planetary sounding radar database. Equations and implementation are detailed in this paper as well as illustrations of obtained results for different instruments (namely, SHARAD and LRS). Our simulation results suggest that the method is able to accurately reproduce the observed clutter in both rough and smooth terrains of the planetary cases discussed in this paper.

1. Introduction

The purpose of this paper is to describe an efficient method to compute radar electromagnetic scattered fields from planetary surfaces. The obtained result is a physical optics simulator which uses analytical integral expressions over triangular surface elements, allowing a significant decrease in computational requirements in comparison to other methods while maintaining the accuracy of the physical optics approach. The equations described in the following sections have been implemented in the framework of planetary sounding radar purpose where emitters and receivers are sets of antennas placed in orbits around planetary objects. Planetary sounding radar is a technique analogous to ground-penetrating radar and synthetic aperture radar (SAR) [e.g., *Ciarletti et al.*, 2003; *Cumming and Wong*, 2005]. The basic principle is to perform electromagnetic remote sensing of planetary bodies with active radar measurements targeting mainly subsurface areas. Several experiments have been designed to study planetary bodies. To this day, two of these instruments are used to study Mars's ionosphere and subsurface, namely, the SHAllow RADar sounder (SHARAD) [e.g., *Seu et al.*, 2004] embarked on the Mars Reconnaissance Orbiter (MRO) probe and the Mars Advanced Radar for Subsurface and Ionosphere Sounding (MARSIS) [e.g., *Picardi et al.*, 2004] aboard Mars Express. A radar instrument, the Lunar Radar Sounder (LRS) [e.g., *Ono and Oya*, 2000; *Ono et al.*, 2010] has also been used to study the Moon as part of the Selenological and Engineering Explorer (SELENE) mission. An additional experiment is being conducted [e.g., *Kofman et al.*, 2007]—the COmet Nucleus Sounding Experiment by Radiowave Transmission (CONSERT)—to study the interior of the comet 67P/Churyumov-Gerasimenko. These radars operate at low carrier frequencies and bandwidth ranging from 1 MHz to few 100 MHz depending on the instruments. Transmitted signals are usually frequency-modulated waveforms, and antennas used in these experiments are mostly dipoles or cross dipoles. Experiment setups (see Figure 1) include either a single emitter/receiver antenna (monostatic) or two antennas (bistatic)—emitter and receiver, respectively—at different locations. Antennas are usually located several hundreds of wavelength away from the planetary body, and the geometry of the problem requires taking the three-dimensional planetary surface into account. Additionally, we assume that planetary atmosphere can be approximated locally by isotropic homogeneous media at the probing radar frequencies

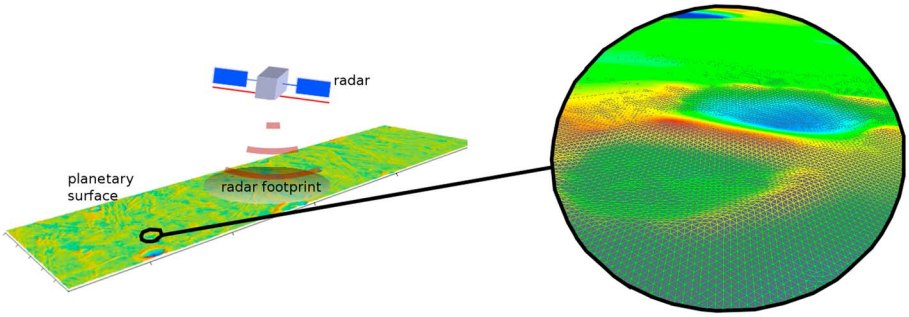

Figure 1. Planetary sounding radar schematic configuration (monostatic). A dipole antenna is mounted on the probe and emits an electromagnetic signal toward the planetary body. The same antenna records scattered and reflected fields from the planetary body (surface and subsurface echoes). The figure also highlights the surface meshing used throughout the paper.

(i.e., constant permittivity and permeability over the area of a single radar acquisition). While in the most general case this would require the ionosphere to be decoupled and treated separately [e.g., *Mouginot et al.*, 2008; *Safaeinili et al.*, 2007], lateral (i.e., not altitude) spatial variations of the dielectric permittivity of the atmosphere and ionosphere at a given acquisition spot can often be neglected in planetary radar. This amounts to considering correlation lengths of the dielectric permittivity of the atmosphere and ionosphere to be much larger than the radar footprint for a single pulse. It is thus possible to use more realistic models with local complex frequency-dependent material property values and local planar-layered model media to account for the atmosphere and ionosphere, for which Green's function analytical expression exists [see *Kong*, 2000]. This point is however beyond the scope of the work described in this paper. Overall, the specific environment for planetary sounding radar explains the choice of a boundary surface formulation, recasting the problem in two dimensions and thus allowing efficient computations of reflected and scattered fields.

When studying planetary sounding radar data, it is important to correctly assess surface echoes (or surface clutter) in order to estimate subsurface contributions in the recorded data. As planetary surfaces are usually the interfaces with the sharpest gradient with regard to material properties (i.e., from the atmosphere to the subsurface), they account for most of the recorded radar echoes. It is thus of paramount importance to be able to model radar surface echoes properly. The technique presented in this paper was designed to go beyond the scope of structural analysis. While planetary radar echoes are commonly used like seismograms to visually recover structural features, we propose to work with signal phases and amplitudes using equations derived from boundary integral expressions of the planetary surface scattered electromagnetic fields. Similar works have been carried out previously using Huygens's principle, in the acoustic approximation [e.g., *Kobayashi et al.*, 2002], for specific setups [e.g., *Fa et al.*, 2009], using numerical integration [e.g., *Plettemeier et al.*, 2009], coupling numerical surface integrations and ray tracing [e.g., *Jin*, 2012; *Zhang et al.*, 2012], or with approximate geometries [e.g., *Nouvel et al.*, 2004]. The latter is currently implemented as a routine to quantitatively assess Mars's ionosphere and Mars's surface permittivity [e.g., *Mouginot et al.*, 2010] from the increasing amount of data acquired with MARSIS. While this technique is quite computation efficient, it requires the planetary body surface to be described as a set of squared facets, which eventually yields discontinuities on the surface and requires to reinterpolate the surface for each acquisition. The technique detailed in this paper does not suffer these shortcomings as it relies on triangular meshing of planetary surfaces. This greatly improves the flexibility and diminishes simulation artifacts of the method while keeping low computation times. The algorithm proposed is thus an improvement to the one in *Nouvel et al.* [2004], as it does not suffer from the main issues with squared facets, namely, (i) surface discontinuities and (ii) reinterpolation of the surface for each radar location. It further allows bistatic configurations. Eventually, such forward modeling of radar surface echoes should allow to quantitatively study topography clutter and permittivity distributions for planetary bodies.

2. Scattered Fields as Surface Integral Equations

Huygens-Fresnel principle (also referred simply as generalized Huygens's principle) states that the field at any point in space $\mathbf{x}_0$ (i.e., the radar location within the planetary plasma environment in our case) is a superposition of spherical waves emanating from a surface S (i.e., the planetary surface in our case) enclosing all the sources and can be directly derived from the Stokes's theorem as a special case which also allows to derive

Stratton-Chu formulation and Green's third theorem. There are several equivalent mathematical representations of Huygens's principle that are important in radiation theory. We present here the fundamental equation we have implemented to compute scattered electric fields.

$$\mathbf{E}_s(\mathbf{x}_0,\omega) = \int_S i\cdot k\cdot \bar{\bar{\mathbf{G}}}(\mathbf{x}_0,\mathbf{x},\omega)\left(\eta\left[\hat{\mathbf{n}}\times\mathbf{H}\right](\mathbf{x},\omega)+\hat{\mathbf{k}}_s\times\left[\hat{\mathbf{n}}\times\mathbf{E}\right](\mathbf{x},\omega)\right)\mathrm{d}\sigma(\mathbf{x}) \tag{1}$$

with

$$\bar{\bar{\mathbf{G}}}(\mathbf{x}_0,\mathbf{x},\omega) = \left[\bar{\bar{\mathbf{I}}}-\hat{\mathbf{k}}_s\hat{\mathbf{k}}_s\right]\frac{e^{ik|\mathbf{x}-\mathbf{x}_0|}}{4\pi|\mathbf{x}-\mathbf{x}_0|} \tag{2}$$

E denotes the electric field, **H** the magnetic field, ϵ the electric permittivity, μ the magnetic permeability, $\hat{\mathbf{n}}$ the unit normal to the closed surface S, **x** a point on S, k the wave number (or spatial frequency) and $\hat{\mathbf{k}}_s$ a unit vector pointing in the scattering direction. $\eta = \sqrt{\mu/\epsilon}$ is the characteristic impedance. We have made use of dyadic notations to express the dyadic Green function $\bar{\bar{\mathbf{G}}}$. This equation is a formal statement of Huygens's principle in the far-field approximation. This expression yields the fields **E** and **H** provided the observer (i.e., receiving antenna) is located within *a homogeneous, isotropic medium*, far from the source and provided the fields on the boundary surface are known. The homogeneous, isotropic medium condition is of course not necessary in theory, but obtaining Green's functions in analytical form is often not feasible. As discussed in section 1, it is also possible to use local planar-layered media to account for the atmosphere and the ionosphere.

3. Discretization of the Boundary Problem

In this section we derive explicit analytical expressions of the boundary equation (1) for a discrete boundary surface. Hence, we assume from now on the boundary surface S to be correctly described as a contiguous set of $N \in \mathbb{N}$ triangular planar facet elements Δ_α such that $S = \{\Delta_\alpha\}_{\alpha\in N}$. This results in a three-dimensional meshed surface (see Figure 1). We further assume that the fields can be expressed as the product of a geometrical term on each facet element $\mathbf{F}^\alpha\left(\mathbf{x}_0,\mathbf{x}_\alpha,\omega\right)$ constant over the facet and of a phase term $e^{i\phi_\alpha(\mathbf{x},\mathbf{x}_0,\omega)}$. It allows us to rewrite equation (1),

$$\mathbf{E}_s(\mathbf{x}_0,\omega) = \sum_\alpha \mathbf{F}^\alpha\left(\mathbf{x}_0,\mathbf{x}_\alpha,\omega\right)\int_{\Delta_\alpha} e^{i\phi_\alpha(\mathbf{x},\mathbf{x}_0,\omega)}\mathrm{d}\sigma(\mathbf{x}) \tag{3}$$

Superscript α denotes here the αth facet variables which are constant over each planar facet element while $\mathbf{x}_\alpha$ denotes the barycenter of the αth facet. It is worth noting that the above equation contains the information on the electric field polarization and is merely the sum of the facet diffracted fields $\mathbf{F}^\alpha\int_{\Delta_\alpha} e^{i\phi_\alpha(\mathbf{x},\mathbf{x}_0,\omega)}\mathrm{d}\sigma(\mathbf{x})$. Computing the phase integral term $\int_{\Delta_\alpha} e^{i\phi_\alpha(\mathbf{x},\mathbf{x}_0,\omega)}\mathrm{d}\sigma(\mathbf{x})$ over a planar facet element is not straightforward. Analytical results can be obtained only in very specific cases. In order to give a generic result for a specified facet element geometry, one has to carry out approximations. We propose to derive analytical expressions for given conditions in the phase term for triangular facet elements.

3.1. Constant Phase Function

The simplest approximation is to consider a constant phase over a facet element $\phi_\alpha(\mathbf{x},\mathbf{x}_0,\omega) = A_\alpha$ with $A_\alpha \in \mathbb{R}$,

$$\int_{\Delta_\alpha} e^{i\phi(\mathbf{x},\mathbf{x}_0,\omega)}\mathrm{d}\sigma(\mathbf{x}) = \Delta S_\alpha e^{iA_\alpha}, \tag{4}$$

where ΔS_α is the surface of the facet element. Any piecewise $\mathcal{C}^1$ complex function on S can be approached through a set of constant over elementary surface elements. In general, this formulation is used to numerically compute Huygens-Fresnel's integral [e.g., *Plettemeier et al.*, 2009; *Kobayashi et al.*, 2002].

3.2. Linear Phase Function

We define $\Delta_\alpha = \{\mathbf{x} \mid a\cdot x + b\cdot y + d = z\}$ with $a \in \mathbb{R}$ and $b \in \mathbb{R}$ and $\mathbf{x} = \{x,y,z\}$, where x, y, and z are the coordinates in a given Cartesian frame. We assume that the phase term can be expressed locally (i.e., over a facet element) as $e^{2jk\left(-a_0\cdot x - b_0\cdot y + d_0\right)}$. This amounts to linear variations in the phase function $\phi(\mathbf{x},\mathbf{x}_0,\omega) = 2k\left(-a_0\cdot x - b_0\cdot y + d_0\right)$. In order to compute the analytical phase integral on a triangular facet, we wish to subdivide the integral domain into right triangle integral domains. This provides rectangular-like integration domains. In addition, we perform a rotation of the frame around the z axis in order to obtain only two triangle integral domains (see Figure 2). Please note that the z axis does not have to be orthogonal to the *ABC*

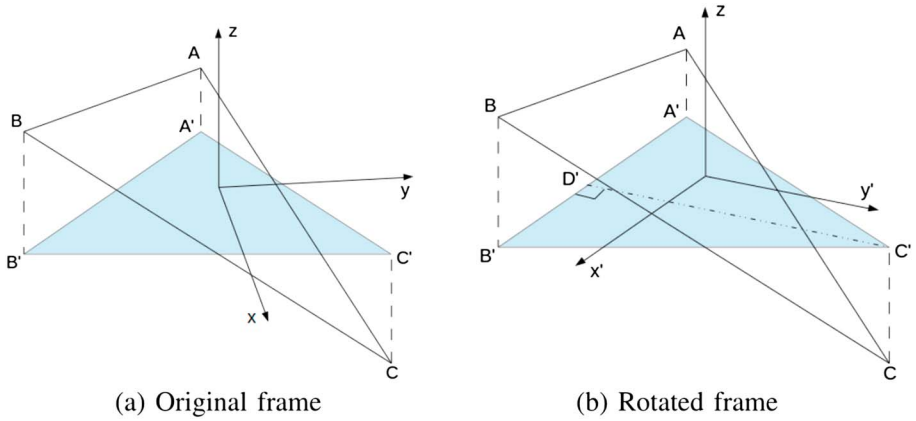

Figure 2. Definition of the local frame in which computations are carried out (from orthonormal local frame *xyz* to orthonormal local frame $x'y'z$). D' is the orthogonal projection of C' on $(B'A')$.

plane but should not lie in it. The phase term in this new Cartesian frame is now $e^{2jk(-a'_0\cdot x'-b'_0\cdot y'+d_0)}$ and $\Delta_\alpha = \{\mathbf{x} \mid a'\cdot x' + b'\cdot y' + d = z\}$.

$$\int_{\Delta_\alpha} e^{2ik(-a'_0\cdot x'-b'_0\cdot y'+d_0)}\mathrm{d}\sigma(\mathbf{x}) = J\cdot\left[\int_{A_{x'}}^{D'_{x'}}\int_{D'_{y'}}^{\alpha_1\cdot x'+\beta_1} e^{2ik(-a'_0\cdot x'-b'_0\cdot y'+d_0)}\mathrm{d}y'\mathrm{d}x' + \int_{D'_{x'}}^{B_{x'}}\int_{D'_{y'}}^{\alpha_2\cdot x'+\beta_2} e^{2ik(-a'_0\cdot x'-b'_0\cdot y'+d_0)}\mathrm{d}y'\mathrm{d}x'\right] \tag{5}$$

with,

$$\begin{aligned} J &= \sqrt{a'^2 + b'^2 + 1}\\ \alpha_1 &= \frac{A_{y'} - C_{y'}}{A_{x'} - C_{x'}}\\ \beta_2 &= C_{y'} - \alpha_2 C_{x'}\\ \alpha_2 &= \frac{B_{y'} - C_{y'}}{B_{x'} - C_{x'}}\\ \beta_2 &= C_{y'} - \alpha_2 C_{x'} \end{aligned} \tag{6}$$

Where A, B, and C are the facet vertices and $A_{x'}$, $A_{y'}$, and A_z are the coordinates of the vertex A in the x', y', z frame. The coefficient J is the Jacobian that arises when changing the integral domain from S (locally Δ_α) to the plane $x'y'\cdot A'B'C'$ is the integral domain on the plane $x'y'$ and is built such that primed points A', B', and C' are the projections of the vertices A, B, and C on $x'y'$ through $\mathbf{z}$, respectively. D' is such that $(C'D') \perp (A'B')$ and $C' \in (A'B')$ (see Figure 2). The analytical expression of the integral is straightforward given the properties of the exponential function,

$$\begin{aligned} \int_{\Delta_\alpha} e^{2ik(-a'_0\cdot x'-b'_0\cdot y'+d_0)}\mathrm{d}\sigma(\mathbf{x}) = J\cdot\frac{e^{2\cdot i\cdot k\cdot d_0}}{(2\cdot i\cdot k)^2\cdot b'_0}\cdot\Bigg[&\frac{e^{-2\cdot i\cdot k\cdot b'_0\cdot\beta_1}}{a'_0 + b'_0\cdot\alpha_1}\cdot\left(e^{-2\cdot i\cdot k\cdot D'_{x'}(a'_0+b'_0\cdot\alpha_1)} - e^{-2\cdot i\cdot k\cdot A_{x'}(a'_0+b'_0\cdot\alpha_1)}\right)\\ &+\frac{e^{-2\cdot i\cdot k\cdot b'_0\cdot\beta_2}}{a'_0 + b'_0\cdot\alpha_2}\cdot\left(e^{-2\cdot i\cdot k\cdot B_{x'}(a'_0+b'_0\cdot\alpha_2)} - e^{-2\cdot i\cdot k\cdot D'_{x'}(a'_0+b'_0\cdot\alpha_2)}\right)\\ &+\frac{e^{-2\cdot i\cdot k\cdot(b'_0\cdot D'_{y'}+A_{x'}\cdot a'_0)} - e^{-2\cdot i\cdot k\cdot(b'_0\cdot D'_{y'}+B_{x'}\cdot a'_0)}}{a'_0}\Bigg] \end{aligned} \tag{7}$$

Should the electromagnetic field vector components be piecewise C^1 complex functions on S, with *slowly* varying absolute values in comparison to the phase term, they can be written as a sum of analytical functions using equation (7) in (3). The reader may note that we have used a unique phase function for all vector field components, but the equations can easily be generalized to each individual component with its own phase term. Figure 3 displays a typical far-field radiated power diagram from a triangular facet element.

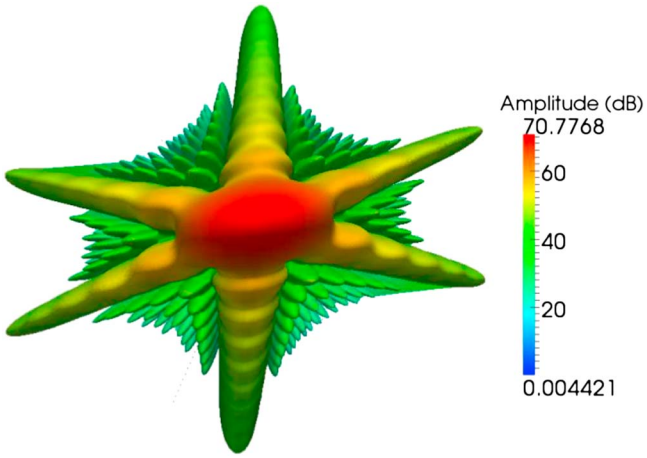

Figure 3. Example of radiated power diagram from a triangular facet element with a linear phase function corresponding to a normal incidence for a given frequency.

It is possible to take into account amplitude variations over a given facet element in addition to phase variations. Appendix A provides the analytical expression of the integral of the phase term modulated by polynomial amplitude functions.

4. Application to Planetary Sounding Radar

In the far-field approximation, the field radiated by an antenna located at $\mathbf{x}_1$ in a homogeneous medium can be written as $\mathbf{E}_i(\mathbf{x},\omega) = |E_i(\mathbf{x},\omega)|e^{ik|\mathbf{x}_1-\mathbf{x}|}\hat{\mathbf{e}}_i$. Let us define $(\hat{\mathbf{k}}_i, \hat{\mathbf{p}}_i, \hat{\mathbf{q}}_i)$ as a local orthonormal system on S with,

$$\begin{aligned}\hat{\mathbf{q}}_i &= \frac{\hat{\mathbf{k}}_i \times \hat{\mathbf{n}}}{|\hat{\mathbf{k}}_i \times \hat{\mathbf{n}}|} \\ \hat{\mathbf{p}}_i &= \hat{\mathbf{q}}_i \times \hat{\mathbf{k}}_i\end{aligned} \tag{8}$$

We now choose to use a Born approximation to express the total electromagnetic field on the planetary surface. With such an approximation, the total field is the sum of the incident field and the local reflected field using Fresnel coefficients as detailed in the next equation. This choice is probably the most limiting factor as it discards multiple reflections and is a mere first-order expansion of the total field. This approximation, when computing the surface integral in electromagnetics, is usually known as physical optics. Fields on the planetary surface S are now expressed as follows:

$$\left[\hat{\mathbf{n}} \times \mathbf{E}\right](\mathbf{x},\omega) = E_i(\mathbf{x},\omega) \cdot \left(\left(\hat{\mathbf{n}} \times \hat{\mathbf{q}}_i\right) \cdot \left[\left(\hat{\mathbf{e}}_i \cdot \hat{\mathbf{q}}_i\right) \cdot \left(1 + R^{\mathrm{TE}}\right)\right] + \hat{\mathbf{q}}_i \cdot \left(\hat{\mathbf{n}} \cdot \hat{\mathbf{k}}_i\right) \cdot \left[\left(\hat{\mathbf{e}}_i \cdot \hat{\mathbf{p}}_i\right) \cdot \left(1 - R^{\mathrm{TM}}\right)\right] \right) \tag{9}$$

$$\left[\hat{\mathbf{n}} \times \mathbf{H}\right](\mathbf{x},\omega) = \frac{1}{\eta} \cdot E_i(\mathbf{x},\omega) \cdot \left(\left(\hat{\mathbf{n}} \times \hat{\mathbf{q}}_i\right) \cdot \left[\left(\hat{\mathbf{e}}_i \cdot \hat{\mathbf{p}}_i\right) \cdot \left(1 + R^{\mathrm{TM}}\right)\right] - \hat{\mathbf{q}}_i \cdot \left(\hat{\mathbf{n}} \cdot \hat{\mathbf{k}}_i\right) \cdot \left[\left(\hat{\mathbf{e}}_i \cdot \hat{\mathbf{q}}_i\right) \cdot \left(1 - R^{\mathrm{TE}}\right)\right] \right) \tag{10}$$

Where R^{TE} and R^{TM} are the well-known Fresnel's coefficients for isotropic media [see *Kong*, 2000]. We further define,

$$\hat{\mathbf{E}}_{\parallel}(\mathbf{x},\omega) = \left(\left(\hat{\mathbf{n}} \times \hat{\mathbf{q}}_i\right) \cdot \left[\left(\hat{\mathbf{e}}_i \cdot \hat{\mathbf{q}}_i\right) \cdot \left(1 + R^{\mathrm{TE}}\right)\right] + \hat{\mathbf{q}}_i \cdot \left(\hat{\mathbf{n}} \cdot \hat{\mathbf{k}}_i\right) \cdot \left[\left(\hat{\mathbf{e}}_i \cdot \hat{\mathbf{p}}_i\right) \cdot \left(1 - R^{\mathrm{TM}}\right)\right] \right) \tag{11}$$

$$\hat{\mathbf{H}}_{\parallel}(\mathbf{x},\omega) = \frac{1}{\eta} \cdot \left(\left(\hat{\mathbf{n}} \times \hat{\mathbf{q}}_i\right) \cdot \left[\left(\hat{\mathbf{e}}_i \cdot \hat{\mathbf{p}}_i\right) \cdot \left(1 + R^{\mathrm{TM}}\right)\right] - \hat{\mathbf{q}}_i \cdot \left(\hat{\mathbf{n}} \cdot \hat{\mathbf{k}}_i\right) \cdot \left[\left(\hat{\mathbf{e}}_i \cdot \hat{\mathbf{q}}_i\right) \cdot \left(1 - R^{\mathrm{TE}}\right)\right] \right) \tag{12}$$

Replacing $E_i(\mathbf{x},\omega)$ with $|E_i(\mathbf{x},\omega)|e^{ik|\mathbf{x}_1-\mathbf{x}|}$ in the previous equations, we obtain,

$$\mathbf{E}_s(\mathbf{x}_0,\omega) = \int_S i \cdot k \cdot \left[\bar{\bar{\mathbf{I}}} - \hat{\mathbf{k}}_s\hat{\mathbf{k}}_s\right] \left(\eta \hat{\mathbf{H}}_{\parallel}(\mathbf{x},\omega) + \hat{\mathbf{k}}_s \times \hat{\mathbf{E}}_{\parallel}(\mathbf{x},\omega)\right) |E_i(\mathbf{x},\omega)| \frac{e^{ik(|\mathbf{x}_0-\mathbf{x}|+|\mathbf{x}_1-\mathbf{x}|)}}{4\pi|\mathbf{x}_0-\mathbf{x}|} \mathrm{d}\sigma(\mathbf{x}) \tag{13}$$

As described in the previous section, we assume the boundary surface S to be correctly described as a contiguous set of $N \in \mathbb{N}$ triangular planar facet elements Δ_α such that $S = \{\Delta_\alpha\}_{\alpha \in N}$. We now have,

$$\mathbf{E}_s(\mathbf{x}_0, \omega) = \sum_\alpha \int_{\Delta_\alpha} i \cdot k \cdot \left[\bar{\bar{\mathbf{I}}} - \hat{\mathbf{k}}_s \hat{\mathbf{k}}_s\right] \left(\eta \hat{\mathbf{H}}_{\parallel}(\mathbf{x}, \omega) + \hat{\mathbf{k}}_s \times \hat{\mathbf{E}}_{\parallel}(\mathbf{x}, \omega)\right) |E_i(\mathbf{x}, \omega)| \frac{e^{ik(|\mathbf{x}_0 - \mathbf{x}| + |\mathbf{x}_1 - \mathbf{x}|)}}{4\pi |\mathbf{x}_0 - \mathbf{x}|} \mathrm{d}\sigma(\mathbf{x}) \tag{14}$$

We further assume field amplitudes to be constant over a facet element and facet extensions to be much smaller than R—with $R = \min\{|\mathbf{x}_0 - \mathbf{x}|, |\mathbf{x}_1 - \mathbf{x}|\}$. Considering the size of the facets we are going to deal with, these assumptions are very realistic in planetary sounding radar. We can now express the field at the surface as the product of a geometrical term $\mathbf{F}^\alpha\left(\mathbf{x}_0, \mathbf{x}_\alpha, \omega\right)$ constant over the facet and of a phase term $e^{i\phi_\alpha(\mathbf{x}, \mathbf{x}_0, \mathbf{x}_1, \omega)}$,

$$\mathbf{E}_s(\mathbf{x}_0, \omega) = \sum_\alpha \mathbf{F}^\alpha\left(\mathbf{x}_0, \mathbf{x}_\alpha, \omega\right) \int_{\Delta_\alpha} e^{i\phi(\mathbf{x}, \mathbf{x}_0, \omega)} \mathrm{d}\sigma(\mathbf{x}) \tag{15}$$

$$\mathbf{F}^\alpha\left(\mathbf{x}_0, \mathbf{x}_\alpha, \omega\right) = i \cdot k \cdot \left[\bar{\bar{\mathbf{I}}} - \hat{\mathbf{k}}_s \hat{\mathbf{k}}_s\right] \left(\eta \hat{\mathbf{H}}_{\parallel}(\mathbf{x}, \omega) + \hat{\mathbf{k}}_s \times \hat{\mathbf{E}}_{\parallel}(\mathbf{x}, \omega)\right) \frac{|E_i(\mathbf{x}_\alpha, \omega)|}{4\pi |\mathbf{x}_0 - \mathbf{x}_\alpha|} \tag{16}$$

$$\phi_\alpha(\mathbf{x}, \mathbf{x}_0, \mathbf{x}_1, \omega) = k\left(|\mathbf{x}_0 - \mathbf{x}| + |\mathbf{x}_1 - \mathbf{x}|\right) \tag{17}$$

We shall now discuss the possibility to express the integral term as an analytical function.

4.1. Constant Phase Function

In this section, we discuss the possibility to use constant fields (amplitude and phase) over each facet element. Assuming the phase term to be constant over the facet element amounts to performing a zeroth-order series expansion of the phase term (i.e., constant phase term over the facet element) with $\phi_\alpha(\mathbf{x}, \mathbf{x}_0, \mathbf{x}_1, \omega) = k\left(|\mathbf{x}_0 - \mathbf{x}_\alpha| + |\mathbf{x}_1 - \mathbf{x}_\alpha|\right)$. In order for this approximation to be valid, facet elements must be small enough with regard to the wavelength. This approximation is equivalent to a numerical integral with each facet element on the mesh corresponding to an elementary surface element Δ_α since both phase and amplitude are constant over a given facet. This method is very easy to implement and most flexible but can be time consuming due to the numerous facet elements needed to describe the surface [*Jin*, 2012; *Kobayashi et al.*, 2002]. Typically, this requires that each element does not exceed $\lambda/10$ in length, which is usually computationally exhaustive [e.g., *Plettemeier et al.*, 2009].

4.2. Linear Phase Function

In this section, we discuss the possibility to use fields with constant amplitude and linear-varying phase over each facet element. The first step is to provide a linearized form of $\phi_\alpha(\mathbf{x}, \mathbf{x}_0, \mathbf{x}_1, \omega)$. We approximate locally the fields—both incident and scattered—as plane waves, and we provide each plane with an orthonormal basis $\{\mathbf{d}_1^0, \mathbf{d}_1^1, \mathbf{k}_1\}_\alpha$ and $\{\mathbf{d}_0^0, \mathbf{d}_0^1, \mathbf{k}_0\}_\alpha$, respectively. $\mathbf{k}_0$ and $\mathbf{k}_1$ are the incident and scattered unit vectors, respectively, along wave vectors which are assumed constant over a facet element. We now express $|\mathbf{x}_0 - \mathbf{x}| + |\mathbf{x}_1 - \mathbf{x}|$ with $\mathbf{x} \in \Delta_\alpha$ and $\tilde{\mathbf{x}} = \mathbf{x} - \mathbf{x}_\alpha$,

$$\begin{aligned} |\mathbf{x}_0 - \mathbf{x}| + |\mathbf{x}_1 - \mathbf{x}| = &\left[\left(\mathbf{x}_\alpha - \mathbf{x}_0\right) \cdot \mathbf{k}_0 + \left(\tilde{\mathbf{x}} - (\tilde{\mathbf{x}} \cdot \mathbf{d}_0^0)\mathbf{d}_0^0 - (\tilde{\mathbf{x}} \cdot \mathbf{d}_0^1)\mathbf{d}_0^1\right) . \mathbf{k}_0\right] \\ &- \left[\left(\mathbf{x}_\alpha - \mathbf{x}_1\right) \cdot \mathbf{k}_1 + \left(\tilde{\mathbf{x}} - (\tilde{\mathbf{x}} \cdot \mathbf{d}_1^0)\mathbf{d}_1^0 - (\tilde{\mathbf{x}} \cdot \mathbf{d}_1^1)\mathbf{d}_1^1\right) \cdot \mathbf{k}_1\right] \end{aligned} \tag{18}$$

We recognize a linear function with regard to vector $\mathbf{x}$. Recalling $\Delta_\alpha = \{\mathbf{x} \mid a' \cdot x' + b' \cdot y' + d = z\}$, the phase function can easily be expressed as

$$\phi_\alpha(\mathbf{x}, \mathbf{x}_0, \mathbf{x}_1, \omega) = 2k\left(-A_0 \cdot x' - B_0 \cdot y' + D_0\right) \tag{19}$$

with,

$$\begin{aligned} A_0 &= \frac{1}{2} \cdot \left(k_{1,x'} - k_{0,x'}\right) + \frac{a'}{2} \cdot \left(k_{1,z} - k_{0,z}\right) \\ B_0 &= \frac{1}{2} \cdot \left(k_{1,y'} - k_{0,y'}\right) + \frac{b'}{2} \cdot \left(k_{1,z} - k_{0,z}\right) \\ D_0 &= \frac{1}{2} \cdot \left(\mathbf{x}_1 \cdot \mathbf{k}_1 - \mathbf{x}_0 \cdot \mathbf{k}_0\right) + \frac{d}{2} \cdot \left(k_{0,z} - k_{1,z}\right) \end{aligned} \tag{20}$$

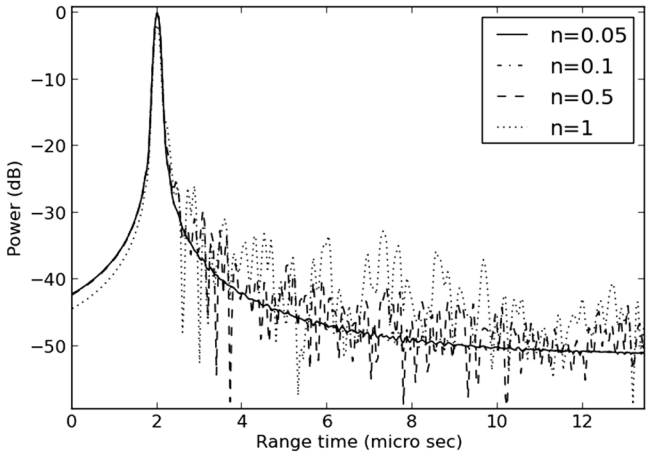

Figure 4. Typical radar responses from flat meshed surfaces with facet edge lengths below $n\sqrt{\lambda R/2}$. Signal distortions can be observed as n increases.

Where $k_{i,x'}$, $k_{i,y'}$, and $k_{i,z'}$, with $i \in \{0,1\}$, are the coordinates of vectors $\mathbf{k}_i$ in the x', y', z frame. Equation (7) then provides the analytical form of the phase integral term. From a functional point of view, the linear phase approximation amounts to performing first-order series expansions at $\mathbf{x}_\alpha - \mathbf{x}_1$ and $\mathbf{x}_\alpha - \mathbf{x}_0$, respectively. In order for this approximation to be numerically valid, facet edges should not exceed $\sqrt{\lambda R/2}$ which corresponds to the Fresnel zone radius in planetary radar sounding. Figure 4 highlights the limitations on facet extension. Facet edge lengths are typically $n\sqrt{\lambda R/2}$. As n increases, the quality of the results decreases. In practice, n was set to 0.2 in most of our simulations. In order to illustrate the accuracy of the simulation with regard to the full waveform signal, we run a very simple case of an isotropic point source emitting an electromagnetic field in the void over a flat conducting surface. The emitted electric field is linearly polarized parallel to the surface with a central frequency at 20 MHz and a 10 MHz bandwidth (see Figure 5). The point source is located 100 km away from the surface, in the far-field region. The simulation results of the computed scattered field at the point source location are compared to the analytical result in Figure 5. Facet edge lengths used to mesh the flat surface where kept below $\sqrt{\lambda R/20}$ (i.e., $n = 0.1$). The simulation results are displayed using dashed lines for both the electric field spectrum amplitudes and the electric field amplitude in time. As can be seen on the figure, the electric field waveform can hardly be differentiated from the analytical solution for both the phase and the amplitude. Please note that the amplitude of the electric field was not normalized to the analytical result which highlights the good energy conservation of the simulation.

A detailed study of the first-order approximation shows Bragg's resonance patterns for structured meshes [e.g., *Nouvel et al.*, 2004] when the constraint limit is reached (see Figure 6). These artifacts are due to the first-order series expansion approximation in the phase term. Using unstructured meshes allows to avoid Bragg's resonance patterns while using larger mesh when the surface is flat, thus increasing computation efficiency (see Figure 6). Figure 6a shows typical radar response from a regularly sampled flat surface. The expected reflected surface echo is clearly seen at 30 μs. Secondary echoes at 40, 50, 75, and 130 μs correspond to Bragg's resonance due to the regular mesh. Echo at 140 μs corresponds to border reflection due to the limited extent of the surface in the simulation. On Figure 6b, typical radar responses from irregularly sampled flat surfaces are displayed with different colors. Similarly, the expected reflected surface echo is clearly seen at 30 μs along with the border reflection at 140 μs. Secondary echoes arising later are artifacts much like Bragg's resonance but adding incoherently.

Interestingly, many techniques making use of Huygens's principle found in the literature naturally relate to the work presented in this section. Fundamentally, their differences arise in the geometry of the facet element used (triangular or square mostly) and in the nature of the quantities associated to each facet used to describe the fields on the surface. In the zeroth-order series expansion case [e.g., *Jin*, 2012; *Plettemeier et al.*, 2009; *Zhang et al.*, 2012], quantities are sets of constant vector (i.e., independent of the position on a facet element) associated to each facet element, which is fundamentally a numerical integration. Whereas in higher-order series expansion cases, quantities are vector fields associated to each facet (i.e., vectors' amplitude and phase can vary with the position where they are evaluated on a facet element). For instance, in our cases (or in *Nouvel*

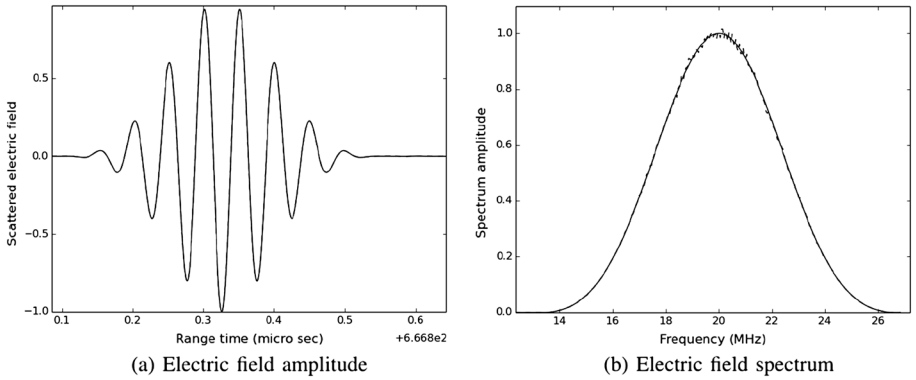

(a) Electric field amplitude (b) Electric field spectrum

Figure 5. Electric field response from a flat surface: (a) time response and (b) spectrum. Simulation results are displayed using dashed lines.

et al. [2004] and *Fa et al.* [2009]) we have used vector fields with constant directions and amplitudes and linear (or parabolic) phase variations with the position over the facet element. Naturally, the incident and scattered field quantities are often chosen of the same nature as that of the total facet field which allows scattered fields to be expressed as a function of the incident field. For instance, in our paper we have used local Fresnel's coefficients to express scattered fields. On the other hand, some authors [e.g., *Ferro et al.*, 2013; *Russo et al.*, 2010] have used local backscattered coefficients to account for local unknown perturbations in the topography (but statistically characterized). Scattered fields have also been computed incorporating subsurface features [e.g., *Jin*, 2012; *Zhang et al.*, 2012]. However, the fundamental difference does not lie in the computation of surface fields (which are supposed to be known in Huygens's principle) but rather in the choice of their local facet expressions (i.e., in the nature of the surface quantities).

5. Implementation

Huygens's principle can be readily used to compute surface echoes from Digital Elevation Models (DEM) with an associated surface dielectric model. In our scheme a first step is dedicated to the triangulation of topography data points. This step can be done using Delaunay triangulation, for instance [e.g., *Delaunay*, 1934]. In order to decrease Bragg's resonance, one might want to resample data. The terrain may contain sharp interfaces between facets on rugged areas which are not necessarily realistic (low resolution of the DEM).

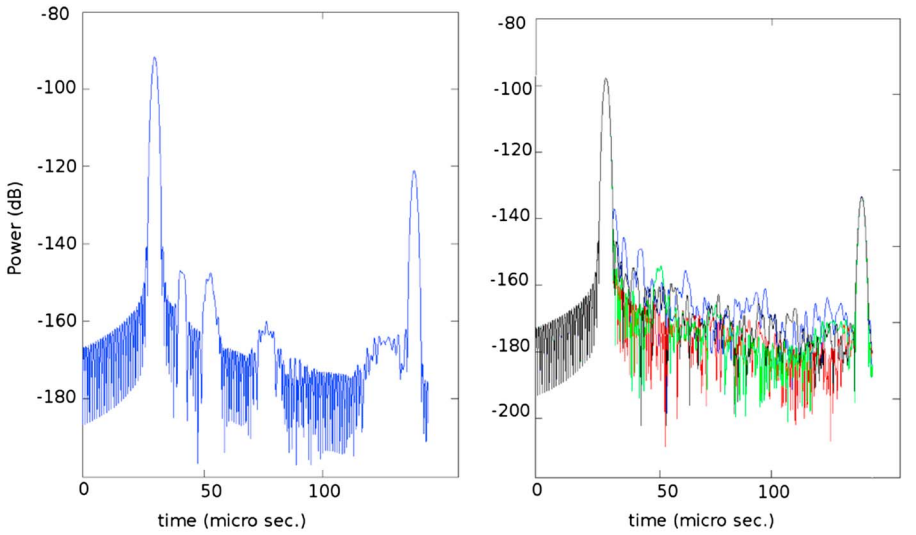

(a) Regularly sampled flat surface (b) Irregularly sampled flat surfaces

Figure 6. Typical radar responses from (a) regularly and (b) irregularly sampled flat surfaces. Regularly sampled surface response displays Bragg resonance patterns unlike responses for irregularly sampled surfaces.

To avoid strong diffraction from facet edges, one may perform a smooth interpolation of the surface through a surface subdivision scheme [e.g., *Schroeder et al.*, 2006]. Further interpolation between DEM data points might be required to match phase integral criterion on facet edge length. We propose here to use on-the-fly Sierpinski subdivision—for the sake of simplicity and efficiency—to match our criterion. Hence, each triangular planar facet obtained after triangulation is subdivided into four homothetic triangular planar facet elements. The subdivision is recursively applied for each triangular facet element until phase integral criterion is matched.

The signal is computed in the frequency domain using the spectrum of the incident electric field. In order to record a given amount of time T, frequency steps should be smaller than $1/T$ as required by Nyquist-Shannon sampling theorem. Hence, the number of frequencies N_f to compute depends on the bandwidth of the signal and on the recording time. It corresponds to $N_f \geq B \cdot T$. For each frequency, the response from a surface area composed of facet elements has to be computed using equation (15). The extension of the surface area contributing to the received signal can be derived from the recording time and the emitter/receiver location. Eventually, we can assess the number of facet elementary responses N to be computed for a single-acquisition geometry. Practically, in planetary radar sounding, all these parameters are closely related and computation time does not vary much from one instrument to another. Assuming a flat surface (i.e., surface subdivision does not depend on the surface topography), the minimum number of facet element N for a single acquisition of a given instrument at distance R to the surface can be derived dividing the area *seen* by the radar by the typical surface of a facet element,

$$N = 2 \cdot \frac{\pi \cdot c \cdot T \cdot \left(R + \frac{c \cdot T}{4}\right)}{L^2}, \tag{21}$$

where L corresponds to facets edge length. Of course, for complex surface geometries, the subdivision may be much higher to accurately describe the surface. In the linear phase approximation, facets edge length corresponds to a fraction of λ, while in the case of the constant phase approximation, facets edge length corresponds to a fraction of $\sqrt{\lambda R/2}$. Hence, the number of facets required in the constant phase approximation is approximately R/λ times the number of facets in the linear phase approximation. Considering that the facet response in the linear phase approximation is about 10 times more computing intensive than that in the constant phase approximation, the computing time in the linear constant phase approximation is approximately $R/(10 \cdot \lambda)$ times the computing time in the linear phase approximation. Typically, in planetary sounding radar, this corresponds to a hundred times the computing time in the linear phase approximation. Another attractive feature of this approach is its ease to parallelize allowing an efficient use of computing resources. Overall, the technique only depends on the central frequency of the signal through limitations on facet extension (order 2 since it is a surface element). In comparison, finite difference time domain methods computation efficiency highly depends on the central frequency of the signal (order 4, three space dimensions and one time dimension). Typically, for MARSIS and SHARAD experiments, a single acquisition represents 3 to 10 s of computation time with two cores at 1.50 GHz. The algorithm proposed is also an improvement to the one in *Nouvel et al.* [2004] as it does not suffer from the main shortcoming of squared facets, namely, (i) surface discontinuities and (ii) reinterpolation of the surface for each radar location. It further allows bistatic configurations.

To incorporate the characteristics of the transmitting and receiving antennas into the scattering equation, we need to modify equations accordingly. This is usually done as a post processing:

$$\begin{aligned} d(\mathbf{x}_0, \omega_0) = -\int_B d\omega jk \mathbf{K}_1(\omega_0 - \omega) \int_S \mathrm{d}\sigma(\mathbf{x}) \mathbf{K}_0(\mathbf{x}_0 - \mathbf{x}, \omega_0 - \omega) \\ \bar{\bar{\mathbf{G}}}(\mathbf{x}_0, \mathbf{x}) \left(\eta \left[\hat{\mathbf{n}} \times \mathbf{H}\right](\mathbf{x}) + \hat{\mathbf{k}}_s \times \left[\hat{\mathbf{n}} \times \mathbf{E}\right](\mathbf{x})\right), \end{aligned} \tag{22}$$

where d represents the complex spectrum of the radar data (i.e., power output of the receiving antenna), $\mathbf{K}_0(\mathbf{x}_0 - \mathbf{x}, \omega_0 - \omega)$ a complex vector which accounts for the antenna gain (antenna pattern, polarization), B is the bandwidth, and $\mathbf{K}_1(\omega_0 - \omega)$ accounts for the electronic instrument response. The code was implemented in C++ using the Eigen library [*Guennebaud et al.*, 2010] and the Visualization Tool Kit (VTK) software system [*Schroeder et al.*, 2006].

It is usually preferable to store the data without any post treatment. This allows multiple signal treatment algorithm to be performed with a single simulated scattered field.

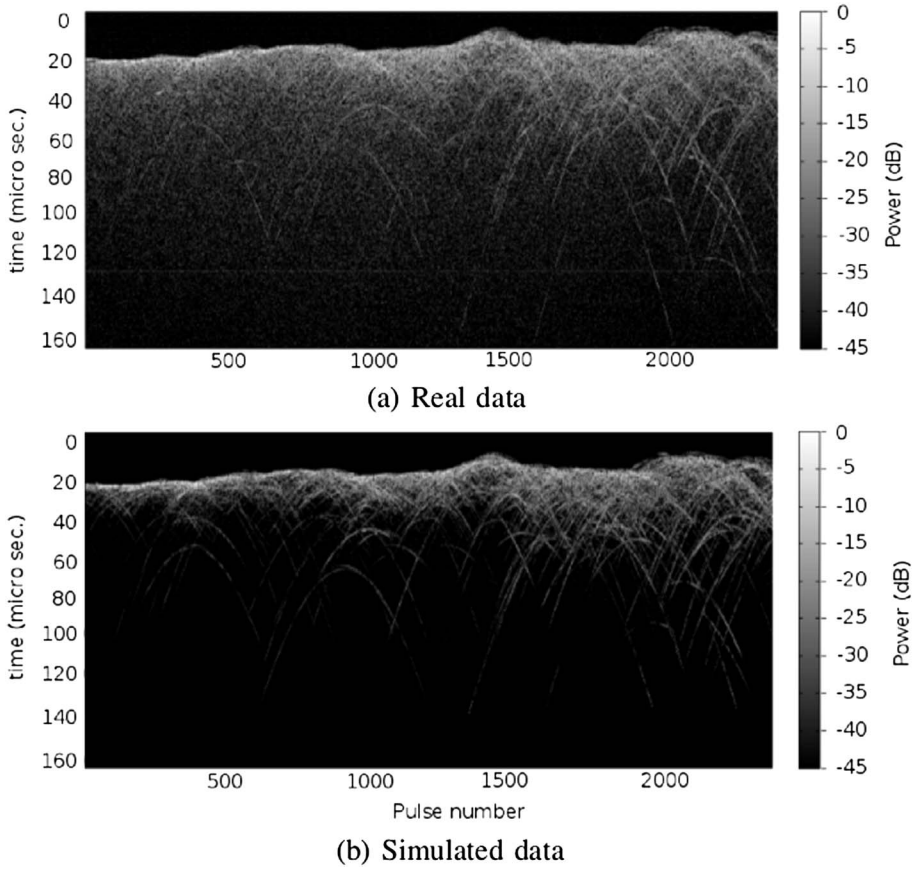

Figure 7. Simulated radar surface echoes for LRS instrument. Color scales are in decibels.

6. Examples

Using the algorithm described previously, surface radar echoes have been computed for several instruments.

We illustrate results with LRS (see Figure 7) using the Lunar Orbiter Laser Altimeter instrument data with 128 pixels per degree to obtain surface topography. Subsurface permittivity was assumed to be a constant in the area. We furthermore assumed a single dipole antenna with a fixed orientation and used hamming windowing for the spectrum. Data are compressed in range [e.g., *Ono and Oya*, 2000; *Kobayashi et al.*, 2002]. The simulation is able to reconstruct radar signals accurately enough from a qualitative point of view in order to reproduce the main structures. The real data seem to contain a diffuse signal which was not reproduced by the simulation. It is likely that this signal is due to surface/subsurface diffusion occurring at much smaller scales than the terrain resolution. Indeed, in our model we assumed Fresnel coefficients over each facet, which does not account for any local diffusion effect.

We also present results for SHARAD instrument (see Figure 8) using the Mars Orbiter Laser Altimeter instrument data (MOLA) with 128 pixels per degree to obtain surface topography. Subsurface permittivity was assumed to be a constant over the areas in both cases. We furthermore assumed a single dipole antenna with a fixed orientation. We applied hamming windowing for visualization. Data are compressed in range. Although we are able to reproduce the main structures, results obtained with SHARAD instrument are clearly not as satisfying as the ones with LRS instrument. This can be explained by a coarser terrain resolution with regards to the signal wavelength as well as possible atmospheric effects and an overall smaller signal to noise ratio. Terrain resolution becomes the main limitation factor as the central frequency of the radar instrument increases to properly reproduce radar signals.

Results indicate a good match between simulations and observation data. The quality of the outputs depends on the validity of the approximations carried out through the previous sections. The far-field approximation is straightforward [e.g., *Kong*, 2000] and will not be discussed here. The main limitation arises in the correctness

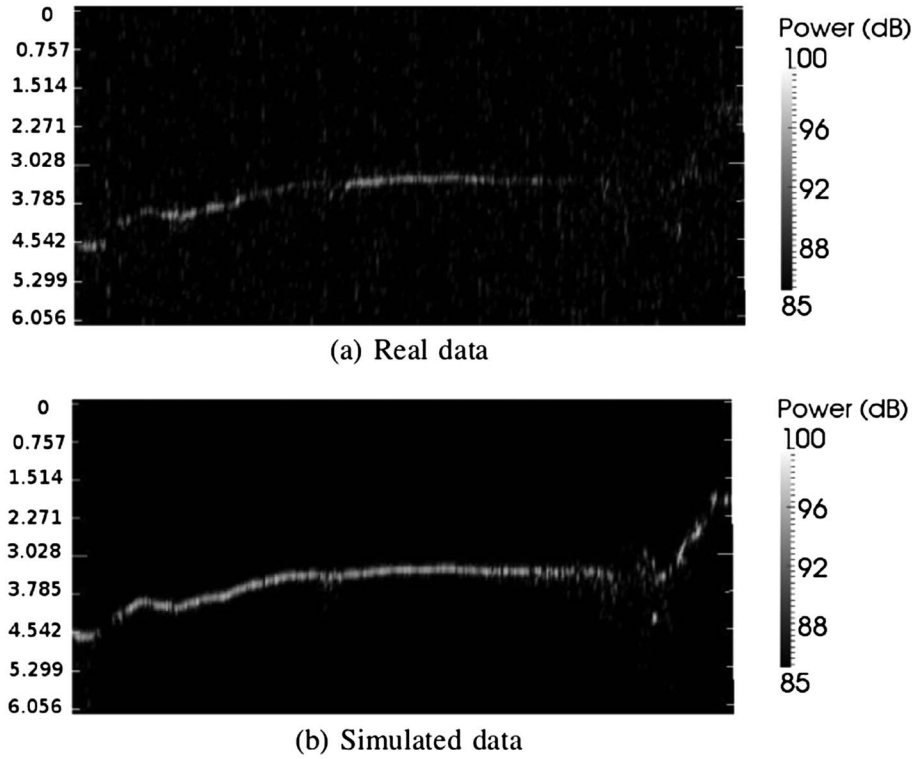

Figure 8. Simulated radar surface echoes for SHARAD instrument (orbit 240301). The central frequency is 20 MHz with a 10 MHz bandwidth. Color scales are in decibels and time scale is in microseconds.

of the surface description as a set of planar facet elements. In order for this assertion to be valid, the deviation from the true surface to the approximate set of facets should be less than a fraction of the radar wavelength. If not, error in the phase term will yield an incorrect assessment of the scattered field (see Figure 6). A correct description of the surface at the wavelength of the probing signal must be used to properly simulate the scattered field. Furthermore, decoupling of facet elements is only valid within sufficiently flat areas. Indeed, if the boundary surface becomes more complex with regard to the topography (for instance, high slopes or microreflectors), multiple reflections will occur affecting the quality of the results [e.g., *Fung and Chan*, 1971; *Fung et al.*, 1992]. Practically, second reflections are often being neglected in planetary sounding radar due to acquisition geometries. However, this issue may arise on heavily cratered terrains or when using high frequencies as slopes tend to steepen at smaller terrain scales.

7. Conclusion

We have presented in this paper an efficient physical optics technique to compute Huygens-Fresnel's integral through a discrete sum of analytical functions. Such tool aims at recovering information on geophysical parameters in planetary sounding radar and should help in the design of future experiments. Nevertheless, the scope of the method extends beyond this specific field of study and can find applications, for instance, in computational electromagnetics since it allows efficient computation of boundary surface integral equations. The use of a surface integral formulation as well as the simplicity and flexibility are major assets for its use in large-scale problems such as planetary radar sounding. Simulated results reproduce well the observed clutter in both rugged and smooth terrains from a qualitative point of view. It should eventually allow a systematic analysis of planetary sounding radar data. Main issues arising with this approach are the difficulty to assess boundary fields—especially when multiple reflections occur—as well as the necessity of an accurate topography description of the surface. Although topographic data from MOLA instrument may be sufficient to reproduce radar surface echoes of MARSIS instrument [e.g., *Mouginot et al.*, 2010], SHARAD instrument requires a much finer topography description. Fortunately, topography data at suitable resolutions are now available on certain areas, thanks to the High Resolution Imaging Science Experiment instrument (HiRISE). Finally, even though Huygens's principle proves to be a powerful formulation for modeling radar surface

echoes, the primary objectives in sounding radar perspective are subsurface parameters. In this framework, the need of an efficient forward modeling of the radar measurements is required to quantitatively analyze radar data. Overall, results presented in this paper allow the prospect of recovering surface properties—such as reflectivity parameter—through classic inversion methods as described in *Araque Quijano and Vecchi* [2010] and *Tarantola* [2005].

Appendix A: Integration of the Phase Modulated by Polynomial Amplitude Functions

In this appendix, we provide the analytical result of the integral over a triangular facet element of the phase term modulated by a polynomial amplitude function. We use a modified expression of the discretized boundary equation (3):

$$\mathbf{E}_s(\mathbf{x}_0,\omega)=\sum_{\alpha}\mathbf{F}_1^{\alpha}\left(\mathbf{x}_0,\mathbf{x}_{\alpha},\omega\right)\int_{\Delta_{\alpha}}\mathbf{F}_0^{\alpha}\left(\mathbf{x}_0,\mathbf{x}_{\alpha},\omega\right)\cdot e^{i\phi_{\alpha}(\mathbf{x},\mathbf{x}_0,\omega)}\mathrm{d}\sigma(\mathbf{x}) \tag{A1}$$

We now assume that $\mathbf{F}_0^{\alpha}\left(\mathbf{x}_0,\mathbf{x}_{\alpha},\omega\right)$ can be expressed in the local frame detailed in Figure 2 as follows:

$$\mathbf{F}_0^{\alpha}\left(\mathbf{x}_0,\mathbf{x}_{\alpha},\omega\right)=\sum_{l=0}^{N}\sum_{m=0}^{N}\mathbf{c}_{l,m}\cdot x'^{l}\cdot y'^{m} \tag{A2}$$

With m and l integers and $\mathbf{c}_{l,m}\in\mathbb{C}$. We now make use of the following equality (p is an integer and $K\in\mathbb{C}$),

$$\int x^p e^{K\cdot x}\mathrm{d}x=\frac{x^p}{K}(-K\cdot x)^{-p}\,p!\,e^{K\cdot x}\sum_{k=0}^{p}\frac{x^k}{k!}+\text{constant} \tag{A3}$$

This allows us to compute the integral term (see Figure 2),

$$\begin{aligned}\int_{\Delta_{\alpha}}\mathbf{F}_0^{\alpha}\left(\mathbf{x}_0,\mathbf{x}_{\alpha},\omega\right)e^{i\phi_{\alpha}(\mathbf{x},\mathbf{x}_0,\omega)}\mathrm{d}\sigma(\mathbf{x})&=\int_{\Delta_{\alpha}}\sum_{l=0}^{N}\sum_{m=0}^{N}\mathbf{c}_{l,m}\cdot x'^{l}.y'^{m}\cdot e^{2ik\left(-a_0'\cdot x'-b_0'\cdot y'+d_0\right)}\mathrm{d}\sigma(\mathbf{x})\\&=J\cdot\sum_{l=0}^{N}\sum_{m=0}^{N}\mathbf{c}_{l,m}\cdot\left[\int_{A_{x'}}^{D'_{x'}}\int_{D'_{y'}}^{\alpha_1\cdot x'+\beta_1}x'^{l}\cdot y'^{m}\cdot e^{2ik\left(-a_0'\cdot x'-b_0'\cdot y'+d_0\right)}\mathrm{d}y'\mathrm{d}x'\right.\\&\quad\left.+\int_{D'_{x'}}^{B_{x'}}\int_{D'_{y'}}^{\alpha_2\cdot x'+\beta_2}x'^{l}\cdot y'^{m}\cdot e^{2ik\left(-a_0'\cdot x'-b_0'\cdot y'+d_0\right)}\mathrm{d}y'\mathrm{d}x'\right]\end{aligned} \tag{A4}$$

Grouping the terms as in equation (7), the analytical result is thus,

$$\begin{aligned}\int_{\Delta_{\alpha}}\sum_{l=0}^{N}\sum_{m=0}^{N}\mathbf{c}_{l,m}\cdot x'^{l}\cdot y'^{m}\cdot e^{K\left(-a_0'\cdot x'-b_0'\cdot y'+d_0\right)}\mathrm{d}\sigma(\mathbf{x})&=e^{K\cdot d}\cdot e^{-K\cdot b\cdot\beta_1}\cdot\left(e^{-K\cdot D'_{x'}\cdot Q}-e^{-K\cdot A_{x'}\cdot Q}\right)\cdot\mathbf{P}_0\\&\quad+e^{K\cdot d}\cdot e^{-K\cdot b\cdot\beta_2}\cdot\left(e^{-K\cdot B_{x'}\cdot Q}-e^{-K\cdot D'_{x'},\cdot Q}\right)\cdot\mathbf{P}_1\\&\quad+e^{K\cdot d}\cdot e^{-K\cdot b\cdot D'_{y'}}\cdot\left(e^{-K\cdot A_{x'}\cdot a}-e^{-K\cdot B_{x'}\cdot a}\right)\cdot\mathbf{P}_2\end{aligned} \tag{A5}$$

with,

$$\begin{aligned}K&=2\cdot i\cdot k\\Q=(a+b\cdot\alpha_1)\mathbf{P}_0&=J\cdot\sum_{l=0}^{N}\sum_{m=0}^{N}\sum_{n=0}^{m}\mathbf{c}_{l,m}\cdot\frac{-m!\,(K\cdot b)^n}{n!\,(K\cdot b)^{m+1}}\\&\quad\times\left[{\alpha_1}^n\cdot(l+n)!\cdot\left(\frac{-1}{K\cdot Q}\right)^{l+n+1}\cdot\left(\sum_{p=0}^{l+n}\frac{(K\cdot Q)^p}{p!}\right)+{\beta_1}^n\cdot l!\cdot\left(\frac{-1}{K\cdot Q}\right)^{l+1}\cdot\left(\sum_{p=0}^{l}\frac{(K\cdot Q)^p}{p!}\right)\right]\\\mathbf{P}_1&=J\cdot\sum_{l=0}^{N}\sum_{m=0}^{N}\sum_{n=0}^{m}\mathbf{c}_{l,m}\cdot\frac{-m!\,(K\cdot b)^n}{n!\,(K\cdot b)^{m+1}}\\&\quad\times\left[{\alpha_2}^n\cdot(l+n)!\cdot\left(\frac{-1}{K\cdot Q}\right)^{l+n+1}\cdot\left(\sum_{p=0}^{l+n}\frac{(K\cdot Q)^p}{p!}\right)+{\beta_2}^n\cdot l!\cdot\left(\frac{-1}{K\cdot Q}\right)^{l+1}\cdot\left(\sum_{p=0}^{l}\frac{(K\cdot Q)^p}{p!}\right)\right]\\\mathbf{P}_2&=J\cdot\sum_{l=0}^{N}\sum_{m=0}^{N}\sum_{n=0}^{m}\mathbf{c}_{l,m}\cdot\frac{-m!\,(K\cdot b)^n}{n!\,(K\cdot b)^{m+1}}\cdot\left[{D'_{y'}}^n\cdot l!\cdot\left(\frac{-1}{K\cdot a}\right)^{l+1}\cdot\left(\sum_{p=0}^{l}\frac{(K\cdot Q)^p}{p!}\right)\right]\end{aligned} \tag{A6}$$

It is interesting to note that the number of exponential functions to compute (i.e., six exponential functions) remains unchanged with the order of the polynomial series. Hence, the complexity of the computation is very close to the one discussed in this paper. It is easy to verify that for $N = 0$, the previous equations are equivalent to equation (7).

Acknowledgments
We gratefully acknowledge Takao Kobayashi for his kind help with LRS data as well as Christoph Statz and Sebastian Hegler for their valuable discussions. A special thank you to Yves Roger for his help with implementing the code. This work was funded by the Centre National d'Etudes Spatiales (CNES) and supported by NASA Planetary Geology and Geophysics Program under grants NNXZ08AKA2G and NNG05GL11G. This research was partly carried out at the Jet Propulsion Laboratory, California Institute of Technology, under a contract with the National Aeronautics and Space Administration. All space mission instruments and topography data can be accessed through NASA and JAXA web portals. The code and the data in general are available upon request by contacting the author via e-mail: (yann.berquin@hotmail.fr).

References

Araque Quijano, J. L., and G. Vecchi (2010), Field and source equivalence in source reconstruction on 3D surfaces, *Prog. Electromagnet Res.*, *103*, 67–100.

Ciarletti, V., B. Martinat, A. Reineix, J. J. Berthelier, and R. Ney (2003), Numerical simulation of the operation of the GPR experiment on NETLANDER, *J. Geophys. Res.*, *108*(E4), 8028, doi:10.1029/2002JE001867.

Cumming, I. G., and F. H. C. Wong (2005), *Digital Processing Of Synthetic Aperture Radar Data: Algorithms And Implementation*, Artech House, Boston.

Delaunay, B. N. (1934), Sur la sphère vide, *Bull. Acad. Sci. USSR*, *7*, 793–800.

Fa, W., Q. Li, and Y. Q. Jin (2009), Simulation of radar sounder echo from lunar surface layer and detection of lunar subsurface structure, EPSC2009-xxxx presented at European Planetary Science Congress 2009, p. 12.

Ferro, A., A. Pascal, and L. Bruzzone (2013), A novel technique for the automatic detection of surface clutter returns in radar sounder data, *IEEE Trans. Geosci. Remote Sens.*, *51*, 3037–3055.

Fung, A. K., and H. L. Chan (1971), On the integral for backscattering from a randomly rough surface, *Proc. IEEE*, *59*, 1280–1281.

Fung, A. K., Z. Li, and K. S. Chen (1992), Backscattering from a randomly rough dielectric surface, *IEEE Trans. Geosci. Remote Sens.*, *30*(2), 356–369.

Guennebaud, G., et al. (2010), Eigen v3. [Available at http://eigen.tuxfamily.org.]

Jin, Y.-Q. (2012), Simulation of radar sounder echoes and inversion of lunar subsurface, paper presented at Annual Meeting of the Lunar Exploration Analysis Group, Greenbelt, Md., 22–24 Oct.

Kobayashi, T., H. Oya, and T. Ono (2002), A-scope analysis of subsurface radar sounding of lunar mare region, *Earth Planets Space*, *54*, 973–982.

Kofman, W., et al. (2007), The Comet Nucleus Sounding Experiment by Radiowave Transmission (CONSERT): A short description of the instrument and of the commissioning stages, *Space Sci. Rev.*, *128*, 413–432.

Kong, A. J. (2000), *Electromagnetic Wave Theory*, EMW, Cambridge, Mass.

Mouginot, J., W. Kofman, A. Safaeinili, and A. Herique (2008), Correction of the ionospheric distortion on the MARSIS surface sounding echoes, *Planet. Space Sci.*, *56*, 917–926.

Mouginot, J., A. Pommerol, W. Kofman, P. Beck, B. Schmitt, A. Herique, C. Grima, A. Safaeinili, and J. J. Plaut (2010), The 3–5 MHz global reflectivity map of Mars by MARSIS/Mars Express: Implications for the current inventory of subsurface H_2O, *Icarus*, *210*, 612–625.

Nouvel, J.-F., A. Herique, W. Kofman, and A. Safaeinili (2004), Radar signal simulation: Surface modeling with the facet method, *Radio Sci.*, *39*, RS1013, doi:10.1029/2003RS002903.

Ono, T., and H. Oya (2000), Lunar Radar Sounder (LRS) experiment on-board the SELENE spacecraft, *Earth Planets Space*, *52*, 629–637.

Ono, T., et al. (2010), The Lunar Radar Sounder (LRS) onboard the KAGUYA (SELENE) spacecraft, *Space Sci. Rev.*, *154*, 145–192.

Picardi, G., et al. (2004), Performance and surface scattering models for the Mars Advanced Radar for Subsurface and Ionosphere Sounding (MARSIS), *Planet. Space Sci.*, *52*, 149–156.

Plettemeier, D., R. Hahnel, S. Hegler, A. Safaeinili, J. Plaut, B. Gaskell, R. Orosei, A. Cicchetti, and G. Picardi (2009), Numerical computation of radar echoes measured by MARSIS during phobos flybys, paper presented at 2009 IEEE Radar Conference, pp. 1–6, Pasadena, Calif., 4–8 May.

Russo, F., M. Cutigni, R. Orosei, C. Taddei, R. Seu, D. Biccari, E. Giacomoni, O. Fuga, and E. Flamini (2010), An incoherent simulator for the SHARAD experiment, paper presented at 2008 IEEE Radar Conference, pp. 1–4, Rome, 26–30 May 2008.

Safaeinili, A., W. Kofman, J. Mouginot, Y. Gim, A. Herique, A. B. Ivanov, J. J. Plaut, and G. Picardi (2007), Estimation of the total electron content of the Martian ionosphere using radar sounder surface echoes, *Geophys. Res. Lett.*, *34*, L23204, doi:10.1029/2007GL032154.

Schroeder, W., K. Martin, and B. Lorensen (2006), *The Visualization Toolkit*, 4th ed., Kitware, New York.

Seu, R., D. Biccari, R. Orosei, L. V. Lorenzoni, R. J. Phillips, L. Marinangeli, G. Picardi, A. Masdea, and E. Zampolini (2004), SHARAD: The MRO 2005 shallow radar, *Planet. Space Sci.*, *52*, 157–166.

Tarantola, A. (2005), *Inverse Problem Theory and Methods for Model Parameter Estimation*, SIAM, Philadelphia, Pa.

Zhang, Y., P. Zhang, S. Cui, X. Zhang, and G. Fang (2012), Imaging of Martian surface and subsurface with high-frequency radar sounder, paper presented at 2012 IEEE International Geoscience and Remote Sensing Symposium (IGARSS), pp. 578–581, Munich, 22–27 July.